A Novel High-Resolution Optical Instrument for Imaging Oceanic Bubbles

Raied Sarmad Al-Lashi, Steve R. Gunn, Eric G. Webb, and Helen Czerski

***Abstract*—The formation of bubbles from breaking waves has a significant effect on air–sea gas transfer and aerosol production. Detailed data *in situ* about the bubble populations are required to understand these processes. However, these data are difficult to acquire because bubble populations are complex, spatially inhomogeneous, and short lived. This paper describes the design and development of a novel high-resolution underwater optical instrument for imaging oceanic bubbles at the sea. The instrument was successfully deployed in 2013 as part of the HiWINGS campaign in the North Atlantic Ocean. It contains a high-resolution machine vision camera, strobe flash unit to create a light sheet, and single board computer to control system operation. The instrument is shown to successfully detect bubbles of radii in the range 20–10 000 μm.**

***Index Terms*—High-resolution oceanic bubble image, imaging oceanic bubbles, oceanic bubble optical instrument, oceanic bubble size distribution.**

I. Introduction

BUBBLES in the ocean play an important role in many marine and atmospheric processes, including air–sea gas transfer [1], [2], marine aerosol production [3], and scavenging of surfactants [4]. Understanding these processes requires accurate measurement of oceanic bubble populations immediately after a wave breaks with adequate spatial and temporal resolution, but such measurements are challenging for several reasons. For winds of 20 m/s, the active whitecap fraction (the area of the ocean surface covered with actively breaking waves at any instant) is commonly of the order of 1%. Therefore even in high winds, actively breaking waves occur relatively infrequently at any single location [32]. The highest void fractions (of order 1%–10%) are associated with very rapid changes in the bubble populations during the first second or so after the wave breaks [5], and it is hard to measure these nonintrusively. Finally, to accurately represent the bubble population, a measurement technique needs to cover a very wide range of bubble radii, from a few microns to a few millimeters [6].

Bubbles entrained by breaking waves have a significant impact on the optical [7]–[12] and acoustical [13], [14] properties of the ocean. A number of techniques have been developed to measure bubble size distributions in the laboratory or in the open sea. However, all of these approaches have their limitations. An ideal technique would be able to measure bubbles in a large radii range, over a large variation in void fraction, with high spatial resolution, have a fast sampling time, and operate in a noninvasive manner [15], [16]. Most of the techniques used to measure bubble populations in the open sea are either optical or acoustical. Every technique has different limitations, and the most important relate to the measured bubble size range and the measureable air void fraction. Acoustical approaches are appropriate for measuring bubble size spectra in low void fractions (below 10^{-4}), and bubble radii from 1 to 500 μm. Previously deployed acoustical sensors in the open ocean have been based on acoustic forward scatter [17], [18], acoustic backscatter [1], [17], [18], and acoustic resonance [1], [6], [15], [17], [18]. However, acoustical techniques cannot be used to measure bubble size distributions at the high void fractions present when the wave first breaks, because of the considerable scattering caused by dense bubble plumes.

Optical instruments are more appropriate for measuring bubble populations with high void fractions and over a wide radii range. A variety of different techniques have been used to generate and detect the light in these devices. Some techniques use a high-resolution image sensor to photograph the illuminated bubbles but low-resolution sensors such as photomultipliers have also been used successfully. The low-resolution sensors were extensively used in laboratory studies, where the bubble plumes are artificially generated. For example, Rojas and Loewen [19], [20] developed fiber optic probes that measure bubble size distributions by using the difference in refractive index between the water and the bubble gas. The probe consists of two optical fibers—one to transmit light and one to receive the light reflected from bubbles—and a signal-conditioning module to infer the void fraction from the reflected light. The range of measured bubble radii was approximately between 1 and 10 mm. However, deployment of these probes in the ocean was challenging. Control of the probe orientation with respect to wind direction is required and they are very sensitive to fouling. Su *et al.* [15] designed a light scattering bubble counter system that used two photomultiplier detectors in the path of a reflected white light

Manuscript received October 14, 2015; revised June 30, 2016 and December 28, 2016; accepted January 22, 2017. Date of publication February 20, 2017; date of current version January 11, 2018. This work was supported by the U.K.'s Natural Environment Research Council under Grant NE/J020893/1.

Associate Editor: J. Jaffe.

R. S. Al-Lashi was with the Department of Electronics and Computer Science, Faculty of Physical Sciences and Engineering, University of Southampton, Southampton SO17 1BJ, U.K. He is now with the School of Food Science and Nutrition, Faculty of Mathematics and Physical Sciences, University of Leeds, Leeds LS2 9JT, U.K. (e-mail: R.Al-lashi@leeds.ac.uk).

S. R. Gunn and E. G. Webb are with the Department of Electronics and Computer Science, Faculty of Physical Sciences and Engineering, University of Southampton, Southampton SO17 1BJ, U.K. (e-mail: srg@ecs.soton.ac.uk; egw@ecs.soton.ac.uk).

H. Czerski is with the Department of Mechanical Engineering, University College London, London WC1E 7JE, U.K. (e-mail: h.czerski@ucl.ac.uk).

Digital Object Identifier 10.1109/JOE.2017.2660099

from the illuminated bubbles inside two cylinders. Their system was based on a dark field specular reflection, where the image forming lens and photomultipliers were positioned at an angle of 125° with respect to the direction of the illuminated light. The two cylinders were illuminated by a system that consists of a Koehler lamp, condensing lens, photo-mask, and projection lens. The sensor responds linearly to bubble radii in the range from 10 to 200 μm. The main drawback of this system is that it requires only one bubble to exist in the sampling volume at any given time and therefore the sampling volume is small (0.012 cm^3) and 10 min or more is required to obtain bubble density measurements.

Photographic techniques based on high-resolution image sensors have previously been used to measure bubble plumes at high void fractions and over a wide radii range in the laboratory and field. Depending on the illumination setup, high-resolution instruments can be classified into two categories: backlit (or light blocking) and direct-light bubble-imaging instruments. The bubble plumes in a backlit system are illuminated from the back and the imaging device is placed opposite the light source. A bright image is captured by the imaging device when no bubbles exist in the measuring volume, while a darker image is obtained when bubbles exist within the optical path [21], [22]. Leifer *et al.* [23] used a combination of two imaging systems to measure bubble radii over the range 15–5000 μm. Wang and Monahan [24] developed a submersible video camera microscope system and tested this in the laboratory to study the effect of salinity on the bubble size distributions. Their system was tested at a depth of 100 mm and bubble radii between 180 and 5000 μm were recorded. The main disadvantage of the backlit system is the difficulty in determining the measurement volume.

In contrast, the illumination system in a direct bubble-imaging instrument forms a light sheet in front of the imaging device. Any bubbles in this sheet will reflect the light to the imaging device and therefore the bubbles are imaged as bright rings on a black background. Stokes and Deane [25], [26] developed a bubble imaging system called BubbleCam to measure ocean bubbles with radii from 200 to 10 000 μm. Their system was based on a camera with a 768 $\times$ 484 pixel resolution and a 10-Hz frame rate, and the image sensor was coupled to the imaging window using a rod-lens boroscope. One disadvantage with this lens is that the full area of the image sensor cannot be used due to the circular image formed by the lens. In addition, the boroscope lens is not telecentric and therefore ambiguity is introduced in the bubble sizes due to the thickness of the light sheet. We note that digital and imaging technology available has improved considerably since Stokes and Deane built their BubbleCam, and that upgrading to modern components can bring considerable improvements in the performance while maintaining the same basic design. For example, the BubbleCam had a relatively long flash duration (2.3 ms) and used a video cassette recorder that restricted the recording time to 2 h, and introduces a mechanical element that may not be robust to vibrations in the ocean during stormy conditions. These limitations can easily be overcome today using modern sensors and data storage. The Stokes and Deane camera provided the initial blueprint for the camera we describe in this paper. However, we tested every aspect of our design independently, investigating a variety of possible geometries and lighting systems for this camera. We concluded that their basic setup of a strobe lightsheet illuminating a known sample volume that was very close to the camera housing is still the best design for this task. The major developments presented in this paper relate to the on-board hardware and software used, which provided considerable additional measurement flexibility, runtime, and resolution and energy efficiency.

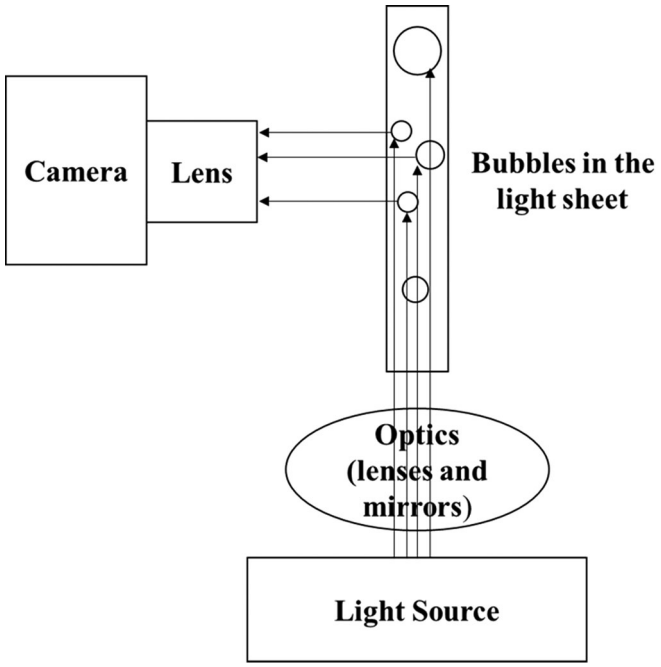

Fig. 1. Diagram showing the imaging principle used. The light source is shown off to the side here, but in our camera system, the light source was behind the camera and 45° mirrors were used to create a perpendicular light sheet.

Improvements on previous optical bubble detectors in terms of sensor resolution, frame rate, optical distortion, recording time, and robustness are required to increase the range of bubble sizes and obtain precise measurements of the bubble size distributions in the ocean. This paper describes the design of a high-resolution bubble-imaging instrument that was successfully deployed in high wind conditions (with hourly averages up to 25-m/s wind speed and 10-m significant wave height) in the North Atlantic Ocean in 2013. The instrument uses a sensitive high-resolution charge-coupled device (CCD) sensor with advanced optics to produce high-quality images. The layout of the paper is as follows: Section II outlines the imaging principles; Section III provides a detailed description of the system hardware and software architecture; preliminary testing is described in Section IV; sample results from the HiWINGS deployment are given in Section V; and the performance of the imaging system is discussed in Section VI.

II. Bubble Imaging Principles

The basic principle of bubble imaging system is shown in Fig. 1. The ocean is dark and therefore a light source is required to illuminate the water sample volume. Lenses and mirrors are used to focus and form a light sheet in front of the imaging

device. Bubbles inside the light sheet will scatter the light out of the sheet and through a lens mounted on the image sensor. The camera depth of field is limited so that only the illuminated bubbles inside the sheet are in focus.

III. Bubble Camera System Design

A. Overview of the Design

Designing an underwater bubble-imaging instrument is a challenging task and entails careful consideration of potentially conflicting requirements. The camera and system hardware need to be mounted in a waterproof housing that can operate to a depth of at least 10 m, and the instrument should be positively buoyant in the ocean. The total available recording time needed to be at least 10 h to allow the instrument to be deployed remotely for extended periods, although this was split between discrete measurement periods so that the instrument could sample at intervals over several days. The instrument was designed to be able to operate over a temperature range of 0 °C–40 °C. The frame rate and image resolution needed to be large enough to show time evolution of the bubble plume during plume creation and the shutter speed should be fast enough to minimize blurring caused by rapid flow past the instrument [25]. The most basic criteria are therefore that the camera frame rate should be higher than 10 Hz and the exposure time should be less than 100 μs. Consequently, it is essential to have a high-intensity light source and image sensor with a good sensitivity to ensure high-quality images. The instrument should be capable of imaging bubble sizes in the range 30–3000 μm. It is essential that the sample volume is close to the instrument to minimize scattering due to bubble plume boundaries between the camera and the measured bubbles [23], [25], but this has to be balanced against the need to make the measurement as nonintrusive as possible. Ideally, the camera will image a bubble plume that is completely unaffected by the camera itself. This is a challenging task because the period of greatest interest is the very turbulent high void fraction period in the first second or so after a wave breaks (with typical turbulent energy dissipation rates up to 10 W/m) [27]. To minimize possible errors in the data introduced by the camera, it is necessary to reduce the flow distortion around the housing so that the camera structure does not itself cause bubble fragmentation or coalescence. In addition, flow through the sample volume must be unimpeded, so that the bubbles sampled are representative of the surrounding bubble field.

Our imaging instrument operates by generating a high-intensity light sheet volume a few millimeters thick in front of a Perspex imaging window (see Figs. 3 and 4). The light sheet thickness is 5 mm on average (we found it to be very slightly thicker in the middle than at the edges). Images are captured by focusing the scattered light through a megapixel telecentric lens mounted on a high-resolution CCD camera. The advantage of using a telecentric lens is that it provides magnification, which is independent of the bubble position within the light sheet. The image resolution was 2048 $\times$ 2048 pixels. To provide a suitable light sheet illumination, a Xenon strobe was connected to a fiber-optic light line. The duration of the strobe pulse is less than 5 μs. This is rapid enough to avoid blurring in the image caused by the bubble motion. The system architecture and the electronic components are explained in more detail below.

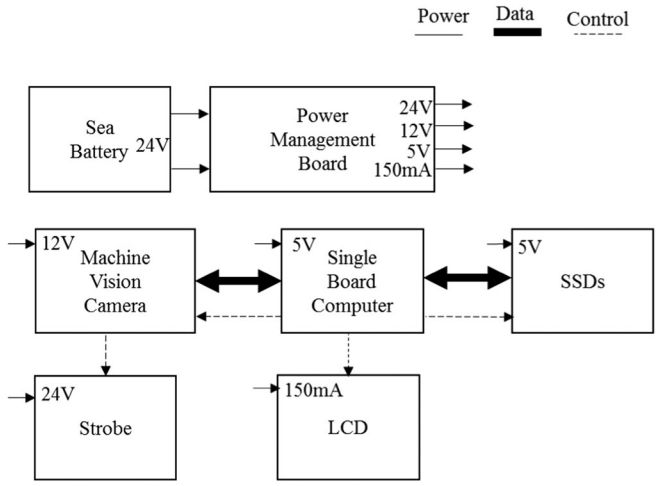

Fig. 2. Block diagram of the instrument architecture.

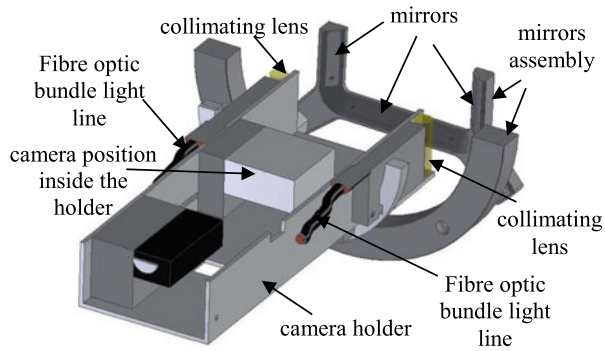

Fig. 3. Diagram of optical pathway in the instrument obtained from taking a cross section of the camera and mirror assembly. The fiber optic bundle connects the strobe to the four light lines, which are coupled into the collimating lenses.

B. System Architecture

The instrument consists of the seven components, as shown in Fig. 2. These are the battery, power management board (PMB) that supplies the required power to the other components, strobe system, machine vision camera (MVC), and single board computer (SBC) that controls the camera recording and saves the images to the solid-state drive (SSD). These are all arranged in a waterproof housing.

1) Light Sheet Formation Unit: The light source needs to provide high intensity over a short duration to avoid blurred images. Three options were considered: Xenon strobe, high-powered LEDs, and a pulsed laser. While LED technology is advancing, they were rejected due to the difficulty with generating a high light output over a short pulse duration. A pulsed laser was rejected due to high cost and power supply complexity. Moreover, laser methods have difficulties with large (nonspherical) bubbles, and high bubbles concentrations [23], [28]. A Xenon strobe is able to meet the requirements, but care is required to ensure that the large current spikes from its power

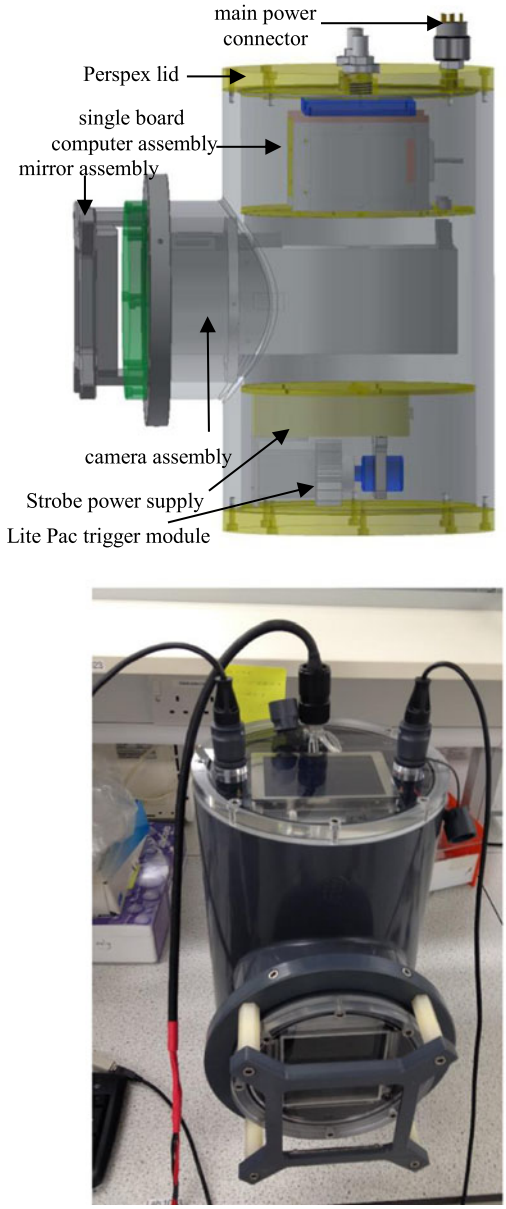

Fig. 4. System hardware components inside housing.

supply do not interfere with the supplies to the other components and that other components are shielded from electromagnetic interference generated by the strobe circuitry. This is achieved by running a dedicated power line from the power source to the strobe, and by placing the strobe assembly in its own chamber at one end of the camera, separated by a steel plate. The chosen Xenon strobe system consists of an Excelitas PS-1120-3 power supply, an FYD-1150B Lite-Pac trigger module, and an FX-1163 high-stability short arc Xenon flashlamp. The flashlamp has an integrated hemispherical mirror that is optimized to direct the light into a fiber bundle. This configuration enables 0.5 J of energy to be delivered to the flashlamp per pulse, which provides a light output of approximately 0.05 J over a 4-μs period. The flashlamp is connected to an optical fiber bundle that splits and terminates at four light lines with collimating lenses, as shown in Fig. 3. These are arranged around the four sides of the camera box tube mount and emit light through the Perspex window. An external mirror assembly containing four 45° mirrors produces a 100-mm $\times$ 100-mm $\times$ 5-mm light sheet, which is parallel with the imaging plane and 2 cm in front of the imaging window.

2) Imaging Device: A JAI (BM-500 GE) MVC that contains a 2/3" progressive scan CCD with 5-megapixel resolution was used to image the scattered light from the bubbles. The CCD sensor has a 2048 $\times$ 2048 resolution with a 3.45-μm $\times$ 3.45-μm cell size. The camera can capture up to 15fps at full resolution and streams the data over Gigabit Ethernet. It is operated at its minimum exposure time of 64 μs, and its output is configured to trigger the strobe at the beginning of the internal exposure enable signal. Due to the high light intensity of the strobe, the effective exposure time is that of the 4-μs strobe pulse. The camera sensor is coupled with a high-resolution telecentric lens (VS-TCM017-110) that is compatible with 5-megapixel sensors. The telecentric lens has an optical magnification of approximately 0.17, *f*-number of *f*/4 and a depth of field of 11 mm. The position of the lens in relation to the light sheet gives a square field of view of approximately 4 cm $\times$ 4 cm.

3) Data Storage Devices: The factors for selecting the data storage device are robustness, storage capacity, form-factor, operating temperature range, and interface bandwidth. The storage device should be resistant to vibration caused by ocean conditions during storms and hence a solid-state drive (SSD) was chosen. The storage requirements for recording at 15 fps, with 2048 $\times$ 2048 image resolution are 226 GB/h. The Crucial M500 SSD was chosen due to its high read/write speed, and small form factor. The capacity of the selected SSD is 960 GB. It is characterized by a 2.5" form factor, 3-Gb/s serial advanced technology attachment (SATA) interface, fast sequential and random read/write, and operating temperature range of 0 °C–70 °C. Two SSDs were employed to increase the camera recording time to approximately 8½ h.

4) Single Board Computer: The requirements for selecting the SBC are small size, low-power operation, passive cooling, Gigabit Ethernet interface, SATA interface, and capability to capture images at the camera frame rate. A Kontron pITX-SP 2.5" SBC (plus) with Intel Atom Z530 processor was selected to meet these requirements. The form factor including all the connectors is 104 mm $\times$ 78 mm. The Kontron is characterized by a 1.6-GHz CPU clock, Gigabit LAN interface, micro secure digital (SD) card slot, two SATA interfaces, 2-GB SDRAM system memory, general purpose input/output (GPIO) interface, and liquid crystal display (LCD) interface. The SBC operating temperature range is from 0 °C to 60 °C. The micro SD card interface allows the operating system to be separated from the data storage. A display board adapter (KAB-ADAPT-LVDS to TTL) was used to interface with a 5.7" VGA LCD display module (HDA570V-G). The LCD module is mounted so that it is visible through the top Perspex window of the camera and provides convenient diagnostic messages in the instrument operation.

5) Power Management Board: The instrument was powered by a 24-V, 40-Ah sea battery, which was located at the base of the spar buoy [29]. A custom PMB was designed to convert and

isolate this power source to run the individual components of the instrument.

The PMB consists of 24–12 V and 24–5-V dc–dc converters, LCD backlight driver, four connectors to supply 5 and 12 V, camera connector, power MOSFET switch circuit, and strobe connector. The 12-V converter supplied the power to the camera and the LCD backlight driver while the 5-V converter supplied the power to the SBC and SSDs. The LCD driver provides a 150-mA current source to illuminate the backlight of the LCD module. The camera connector supplies power to the camera and connects the camera output with the strobe trigger input. The power to the camera is controlled by a MOSFET connected to the GPIO of the SBC to enable the camera to be powered down from software when not in use, to conserve power. The strobe connector supplies power to the strobe flash unit and connects the strobe trigger input to the camera output to synchronize the strobe firing with the camera shutter. The total current drawn by the PMB in normal operation is around 1.5 A.

A programmable timer and a relay were used to control the power supplied to the instrument, enabling a full power shutdown when the instrument was not acquiring images. This is advantageous in long deployments where the capture time is distributed over different periods, conserving power, and reducing the effects of temperature increases inside the housing.

6) Housing: The camera housing should be of a suitable design to enable straightforward connection to the spar buoy. It needed to be watertight to a depth of 10 m, and extremely robust because of the severe conditions possible at the sea. The housing should provide a large enough optical window for the camera field of view to image the bubble plumes in the light sheet. The camera housing was constructed from an 8-kg polyvinyl chloride (PVC) reducing tee with diameter 225 mm $\times$ 160 mm, as shown in Fig. 4. It has a cylindrical T-shape that eases mounting on the spar buoy, with the use of brackets. The housing is divided into three chambers, which are separated by two steel discs. The top chamber contains the bulk of the electronics, the middle chamber contains the optics and imaging components, and the bottom chamber contains the strobe assembly. The mirror assembly was mounted outside the housing and in front of camera optical window, as shown in Fig. 4. The fiber optic bundle emerges from the strobe chamber and terminates at four collimated lenses in the camera assembly. O-rings were used to seal the 1" Perspex discs with the housing windows.

The main limitation of the PVC housing is potential for the electronics to overheat because of the poor thermal conductivity of PVC. This could be minimized further by adopting a metal housing. However, here a programmable timer was used that switches on the power for 45 min every 2 or 3 h. In combination with the ocean temperature (which was generally close to 8 °C during the 2013 deployment), this ensured that the instrument operated correctly. As with any housing of this nature, care must be taken to ensure that condensation does not form within the instrument during operation. There are two common approaches that can be adopted: First, provide a valve to allow the chambers to be flushed with nitrogen before deployment; and second, use a desiccant inside the housing. Here, the simpler approach of using a good desiccant was adopted, by placing molecular sieve inside the housing.

C. Software

1) Operating System: Linux was selected as the operating system for the SBC, due to the flexibility in configuring the running processes and its open source nature. The Debian squeeze distribution (version 6.0.7) was selected for stability. The operating system was installed on an 8-GB micro SD card enabling it to be isolated from the SSDs holding the image data. These can then easily be exchanged without affecting the operating system. The disadvantage of a micro SD is that care must be taken over the maximum number of write cycles. We choose not to create a swap partition to keep the number of write cycles to the micro SD at a minimum. This does not affect the performance because the 2-GB RAM is sufficient to hold all running processes and programs for the camera.

An executable bash script was written to start the camera capture program autonomously and immediately after boot up. The program runs for 45 m, and after terminating a "poweroff" command is executed to shut down the SBC. The programmable timer is configured to shutdown power to the whole instrument a few minutes later.

2) Power Control: The Kontron-supplied JIDA API was used to access the hardware features of SBC, and control power to the MVC and backlight LCD.

3) Image Acquisition Control: A C++ program was written using the JAI SDK to control image capture. Camera features such as exposure time, frame rate, and packet size were stored in a separate configuration file for flexibility. The capture program begins by reading the settings from the configuration file and initializing the camera. The camera starts the acquisition by assigning the internal exposure enable signal to the camera output port to trigger the strobe. To ensure the maximum possible frame rate, the images are streamed and saved in a raw format.

IV. Calibration

This section describes the calibration procedures that were carried out before deployment to ensure that the instrument would operate successfully in the ocean conditions.

A. Bubble Size Detection Range

A reliable automated algorithm for bubble extraction was developed to process images, and the details of the testing and calibration of that algorithm are set out in a separate paper [33]. We will only provide a basic overview here, limited to the details relevant to camera calibration. The bubble extraction algorithm was based on a modified Hough transform and was evaluated using both synthetic and real images. A model was used to generate bubbles with radii ranging from 1 to 50 pixels and randomly position them in the synthetic images. The algorithm extracts bubble sizes as small as 1 pixel in radius (2 pixels in diameter), but the extracted bubbles are divided into two categories. "Ring" bubbles are those with a clear black area inside the white bubble edge. "Disk" bubbles are solid, without a clear dark core. The "ring" bubbles are the more reliable measurement, but the count of "disk" bubbles may also provide useful information if used in context. The algorithm was

also evaluated on 80 real images and was verified to successfully extract bubbles robustly. Final calibration was performed by imaging a known grid in the light sheet plane to determine the correct scaling factor from Hough space to bubble size.

The results shown in this paper are the "ring" bubbles only. The results of the synthetic image tests showed that bubbles with a radius of 2 pixels could be reliably identified as "ring" bubbles, showing a clear edge with a darker patch in the center. In the images collected during the HiWINGS cruise, 1 pixel had a width of 20 μm. A bubble image that was 4 pixels in diameter and 2 pixels in radius (and therefore a 40-μm radius bubble) was easily identified by the algorithm. The algorithm could also detect bubbles represented by one dark pixel surrounded by 4–8 lighter ones (in a 3 $\times$ 3 grid). This gives a minimum possible detectable bubble radius of 20 μm, so we include these bubbles on the results plots. However, the number of bubbles in this smallest bin should be treated with some caution as the distribution between "ring" and "disk" will be more biased toward the "disk."

The maximum bubble size that can be measured by this device is of the order of 10 mm radius (since the field of view is 4 cm $\times$ 4 cm). However, we did not see any bubbles of this size during sea trials. The range of bubbles detectable by this camera is therefore 20-μm radius up to 10-mm radius.

B. Maximum Detectable Air Fraction

There is considerable interest in making bubble size distribution measurements inside actively breaking waves, and so one measure of any bubble imaging system is the maximum void fraction it can reliably measure. To estimate this, we took images collected at sea as the buoy was being lowered into the water, when the camera was close to the surface and splashing was generating high-bubble void fractions. These were the highest void fraction images that we could find in our sea data. We manually counted the bubbles visible in the light sheet in these images (carefully excluding bubbles that were outside the light sheet but still partly in focus), and estimated their volume based on their maximum and minimum diameter (since many of the imaged cross sections were elliptical). From this, we estimate that the maximum measureable void fraction is between 5% and 10%, depending on the bubble sizes that are contributing to the air volume.

C. Perturbation of Bubble Size Distribution

This camera was mounted on a free-floating spar buoy (11 m in length), during the field campaign for which it was first used. A spar buoy is not the ideal platform for detailed near-surface bubble measurements, but it was the only option available for this field campaign. The highest void fractions are found within the first meter of the sea surface, and to sample them properly, a surface-following platform is needed. A spar buoy does not follow the surface—it should hold its position as the waves move water up and down around it, so the actual depth of the camera on these deployments was changing with time. The spar buoy did provide one advantage in this case: An upward-pointing sonar was mounted at the base of the buoy to scan the water in front of it, allowing us to interpret local bubble measurements from the camera in the context of whole bubble field. More information about the buoy can be found in Pascal *et al.* [29], including an assessment of its movement in different sea states. It should be noted that, although a spar buoy is designed to allow waves to move past without affecting the buoy position in the water column, for the very large waves encountered during these deployment (with significant wave heights approaching the total buoy length), the spar did follow the surface to some extent in the highest seas. Sonar and wavewire measurements gave us measurements of the camera position in the water column at all times, allowing us to take this into account as we interpret the data.

The camera was mounted so that it was always facing into the wind. If an oncoming wave was breaking actively just in front of the buoy, the buoy instruments would stay in the same patch of water as the evolving bubble plume, so there was no large-scale flow past the buoy because it moved with the water. However, turbulent eddies with length-scales less than the size of the buoy could cause the seawater to have a significant flow speed relative to the camera. This carries the risk that the camera structure (which protruded from the buoy on the windward side) could generate fluid flow distortions of its own. For a reliable measurement, the camera structure should not be responsible for any additional bubble coalescence or fragmentation, as this could change the local bubble size distribution. In addition, it is important that seawater can flow freely past the camera, so that bubbles do not get trapped close to or diverted away from the sample volume.

Because the buoy was free floating, the potential relative flow speeds are not as high as they might be for a camera attached to a rigid platform that was not moving with the large-scale flow. However, we carried out basic studies of the fluid flow around the camera housing, and the behavior of bubbles close to the housing, to assess whether flow distortion could have a significant effect on the measurement.

The studies were carried out in two ways. The first was the generation of large bubble plumes (using a tipping bucket method) close to the camera while it was in a large aquarium. This was done extensively during the early camera tests, and no evidence of bubble trapping or extra bubble fragmentation or coalescence was seen. Bubble size distributions were monitored both with the camera itself and external cameras. In addition, small bubbles generated using an aquarium bubbler were used as tracers to follow the fluid flow around the camera. We did not observe any eddies or vortices forming around the camera, and it was notable that bubbles flowed very easily through the sample volume without being trapped or impeded. The low flow distortion is partly due to the hydrophobic nature of the housing material, which made the boundary layer very thin. The cylindrical shape of the housing also helps—the fluid flow splits easily around the housing with very few eddies appearing. We could not detect any dead zones or regions of additional turbulence. However, we were not able to test the highest flow speeds that might be expected in open-ocean conditions. Because our open-ocean measurements were carried out approximately 2 m below

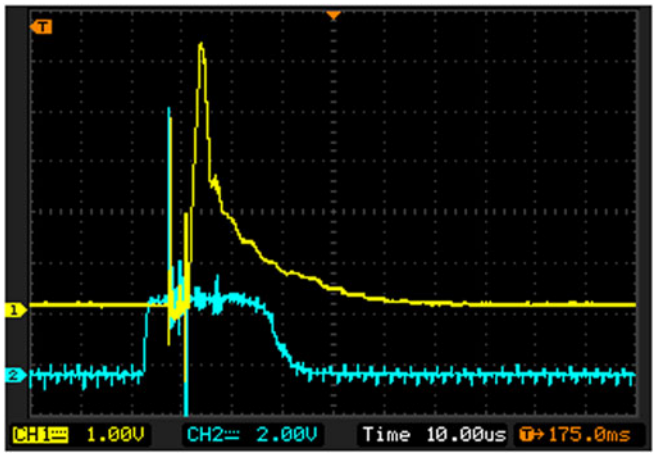

Fig. 5. Photo diode voltage (top) synchronized with camera exposure output signal (bottom).

the ocean surface on a free-floating buoy, we feel confident that flow distortion is not a significant problem for our open-ocean measurements. However, we acknowledge that it would be ideal to implement a full computational fluid dynamics flow model (potentially backed up by laboratory tests with better tracers) before this camera is used on a fixed platform with much higher relative flow speeds.

D. Light Sheet

Tests were undertaken to measure the light sheet duration and thickness. The light duration was measured using a photodiode and an operational amplifier, converting the light into an electrical signal that was displayed on an oscilloscope, as shown in Fig. 5. It can be seen that the flash duration is approximately 4 μs and is synchronized with the camera exposure output signal.

To keep the light sheet thickness small and to minimize the effect of secondary reflections from bubbles between the light sheet and imaging window, the mirror assembly was adjusted to be 0.5 cm away from the imaging window. The camera position was then adjusted in the assembly to ensure that the light sheet sat within the depth of field of the telecentric lens. A 45° prism was then placed against the optical window to redirect the light sheet on to the imaging sensor. Images of the reflected light sheet cross section were taken with the prism at different positions and orientations on the optical window (an example is shown in Fig. 6). This confirmed the thickness of the light sheet to vary slightly with an average width of approximately 5 mm.

E. Hardware

To test the stability of the instrument tests were conducted in a cold store with a controlled temperature of 3.5 °C to simulate the temperature in the North Atlantic Ocean. The instrument was left in the cold store overnight to bring its temperature down to approximately 5 °C. A 12-m power cable was used to simulate the cable from the battery to the instrument mounted on the buoy. The dc voltages at the connectors of the PMB were measured. The instrument was left running under water to

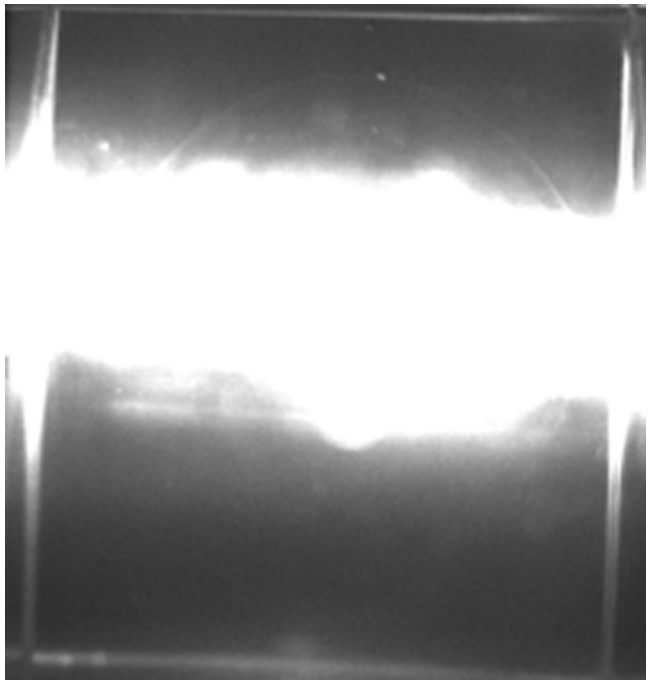

Fig. 6. Light sheet imaged via a 45° prism. Using measurements like these, the light sheet was found to be 5 mm wide. The scale of this image is 15 mm on each side.

capture images over 5 h. The internal case temperature gradually increased from 4.7 °C to 31.6 °C after 5 h, but remained within the safe operating region. If the CPU temperature exceeds 65 °C throttling of the processor clock can cause dropped packets in the image capture. The images were successfully acquired and stored on the SSDs. These tests were successfully repeated for different capture intervals.

V. North Atlantic Ocean Deployments

The instrument was successfully deployed as part of the Hi-WINGS campaign in the North Atlantic Ocean in 2013. Some of these deployments were during stormy conditions, where the winds reached speed of up to 30 m/s for short periods (the highest hourly average was 27 m/s). There were seven deployments in total, ranging from a few hours to a few days in length. The aim of campaign is to study the impact of wave breaking and bubble processes on air–sea gas exchange during storms. The instrument was mounted approximately 2 m beneath the ocean surface on a spar buoy [28], as shown in Fig. 7. A number of complementary instruments were also attached to the buoy including an optical imaging instrument mounted at the top of the spar buoy to image the whitecaps on the ocean surface. During the deployments, the buoy was left floating freely in the open sea with the bubble imaging instrument capturing frames over 45-m intervals. A timer controlled the intervals and there would typically be around ten over a deployment.

Fig. 8 shows a sample image collected by the instrument when deployed in its autonomous configuration. The outline of the bubbles appears as points of high intensity in the images; small

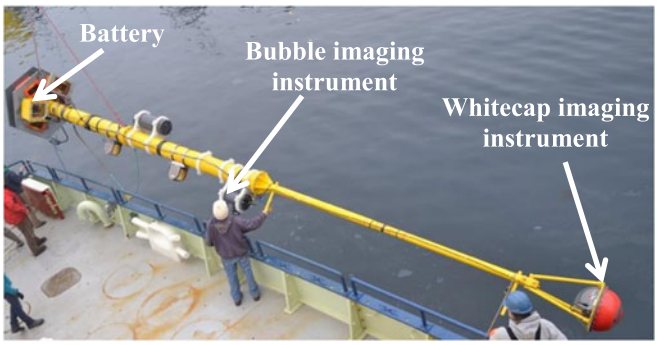

Fig. 7. Bubble imaging instrument position on the spar buoy. In calm water, the waterline would be halfway down the thin "neck" of the buoy, where the black mark is visible on the picture.

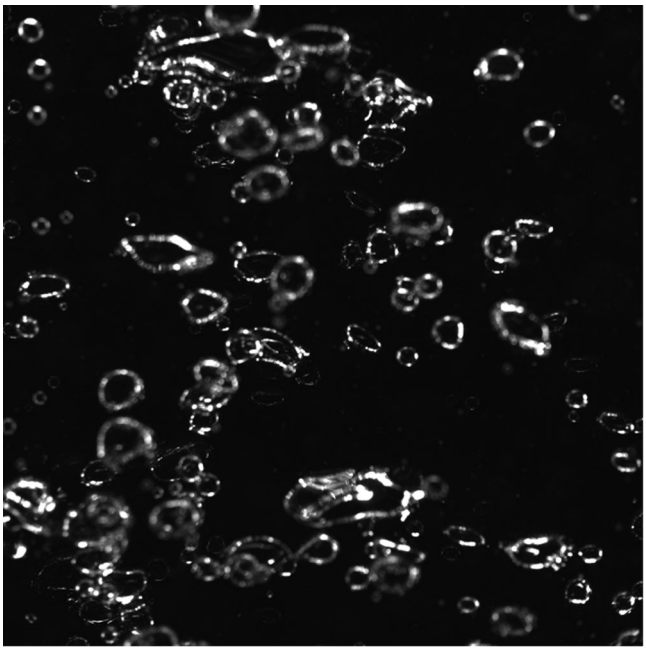

Fig. 8. Spherical and nonspherical bubbles, imaged at very shallow depths (<1 m) when the buoy was being lowered into the water. The picture shows the entire sample volume, 4 cm on each side.

bubbles are spherical while large bubbles tend to be nonspherical due to the effects of surface tension [30].

Even in complex images that are unsuitable for automated bubble extraction, the bubble images can still provide important information: Fig. 9 shows a complex image of air entrainment within a breaking wave during bubble plume formation, which can give useful insight into bubble formation mechanisms [26]; Fig. 10 shows how bubbles behave to form a foam patch on the surface of the ocean.

VI. Results

Bubble size distributions can be determined from the image frames by extracting the size of each individual bubble using an automated image extraction algorithm based on the Hough transform. Full details of the extraction algorithm are discussed in Al-Lashi *et al.* [33]. For the purpose of this paper, it is sufficient to say that the automated algorithm can extract bubbles as small as between 1 and 2 pixels in radius, which is equivalent to a bubble radius between 20 and 40 μm. The sample volume of water was approximately 40 mm $\times$ 40 mm $\times$ 5 mm.

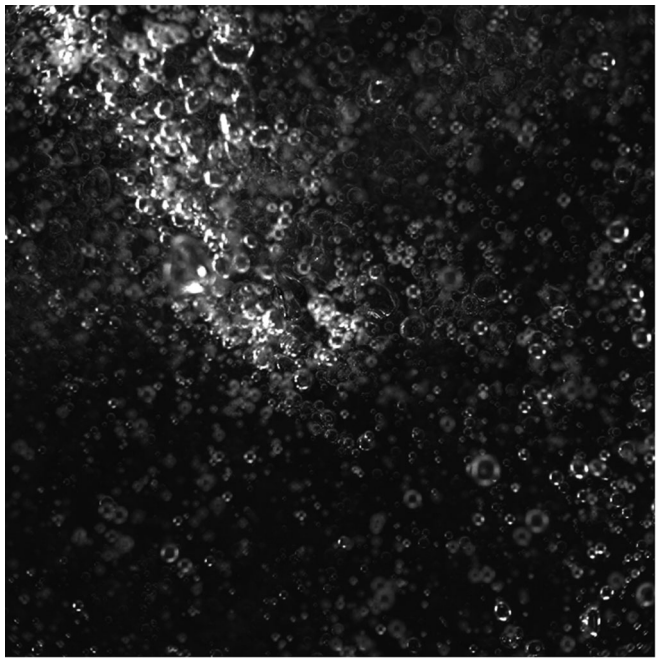

Fig. 9. Dense bubble plume, imaged as the buoy was being lowered into the water. The image is 4 cm on each side.

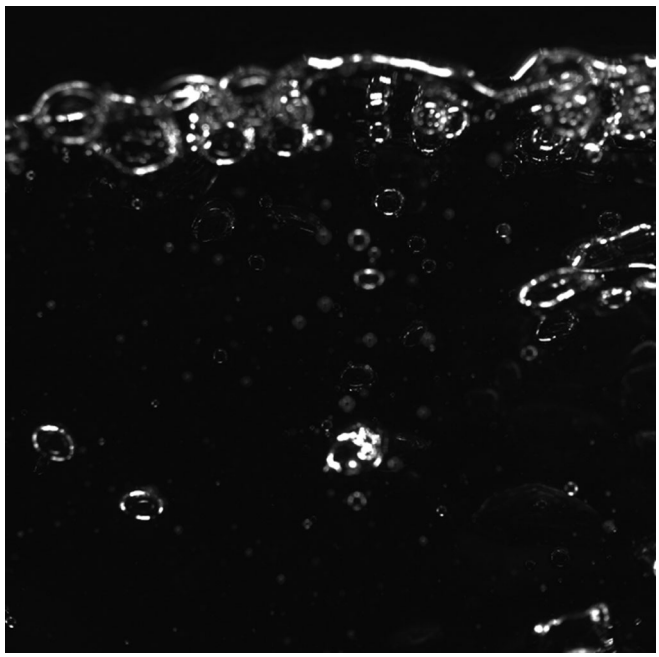

Fig. 10. Image showing a cross section through the air–water interface. A population of bubbles accumulated at the water surface is visible, along with some rising from below.

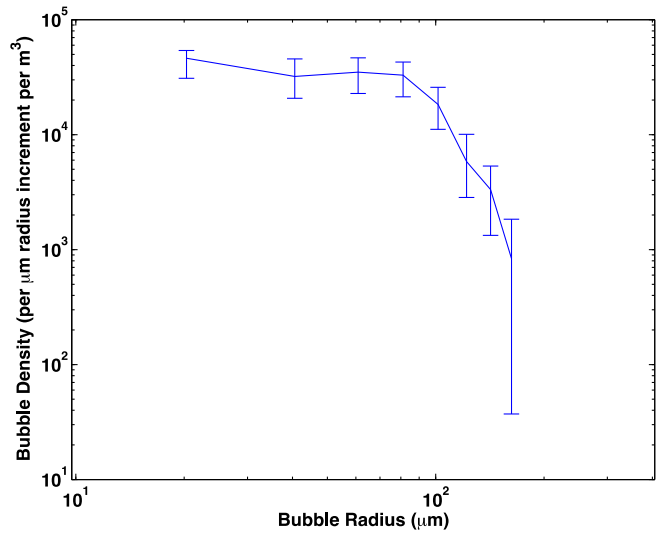

Fig. 11. Bubble density captured by the instrument from a short (1 s) high activity sequence in one of the North Atlantic Ocean deployments in 2013.

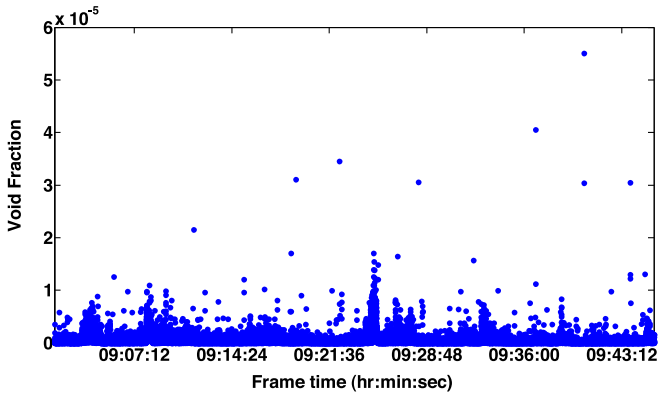

Fig. 12. Void fraction as function of time for the bubble size distribution shown in Fig. 11.

The camera was configured to capture images for 45 min every 3 h during six days of deployment in the open ocean in October and November 2013. The results presented here use 40 000 images collected over a 45-min period, where the wind speed was 65 kn and the average significant wave height was 11 m. All measured bubbles were smaller than 500 μm in radius and more than 95% were less than 100 μm in radius.

Fig. 11 shows the bubble size distribution measured during a 1 s period corresponding to the area of high activity in Fig. 12 around the 09:25:00 UTC mark. Errors bars were calculated taking into consideration the radii estimation error, bin sample size, occlusion and slicing effects. A marked knee in the curve is observable at around 80 μm; above this value, the bubble density is approximately proportional to the radius to the power -5.

Fig. 12 shows the total volume of air per measuring volume of water (void fraction) in each image versus frame time. The measuring volume of the light sheet is $40 \times 40 \times 5$ mm^3, with an uncertainty of $\pm 20\%$ due to the difficulty in estimating the light sheet width.

TABLE I
PERFORMANCE COMPARISON OF THE BUBBLE IMAGING INSTRUMENTS USED TO MEASURE BUBBLE SIZE DISTRIBUTIONS

Bubble imaging instrument	Al-Lashi *et al.*	Stokes and Deane	Leifer *et al.*
Sensor resolution (pixel)	2048 × 2048	768 × 484	752 × 582
Bubble size range (μm)	20–10 000	200–10 000	15–500
Max void fraction	0.1	0.27	
Imaging volume	square	circular	rectangular
Imaging volume size	$4 \times 4 \times 0.5$ cm^3	3.65×0.3 cm^3	$2 \times 0.29 \times 0.19$ cm^3
Frame rate (Hz)	15	10	
Effective exposure time (μs)	4	2300	1000
Recording time	8.5 h	2 h	15 min

The empty cells in the table indicate that the information is not available in the corresponding published papers.

VII. DISCUSSION

A. Bubble Size Distribution

The limit on the measured bubble size range has important implications for the calculation of total void fraction of bubble plumes. Smaller bubbles in the plumes dominate the void fraction when the increase in number of bubbles is larger than the bubble radius to power of -3. However, the plumes would be dominated by larger bubbles when the increase is less than the radius to power of -3 [25]. However, in practice, it has been found that the largest bubbles do not make the most significant contribution to void fraction after the first few seconds of the plume. The size range detectable by this instrument is therefore likely to provide accurate void fraction measurements. The limit to the minimum detectable bubble size is determined by the sensor resolution of the imaging device and the magnification of the lens. The minimum detected bubble radius of the instrument was around 20 μm. This is equivalent to Rayleigh resolution limit for this type of optical imaging system [25]–[31]. It is possible to adjust the camera optics to obtain greater magnification to image smaller bubbles. However, this reduces the imaging volume, which limits the measurement of larger bubbles.

Another important consideration is the image capture rate, which is 15 Hz in the current instrument configuration. This is not fast enough to follow the details of individual bubble formation processes in the turbulent water as the wave breaks, but it is sufficient to follow the general evolution of the plume.

Detecting the scattering of light at the boundaries of bubble plumes requires an invasive instrument that operates within the interior of the plume. Although such an instrument may affect the bubbles around it, the instrument orientation normal to the water flow assists in reducing these problems. The PVC tee housing was robust and reliable in protecting the hardware components against water leakage during stormy deployments.

The temperature inside the housing was minimized by using a programmable timer to reduce the duty cycle of the instrument of long deployments. Should the device be required to operate in warmer waters and/or over a longer continuous duration, a stainless steel housing could be used to improve heat dissipation.

B. Instrument Performance

The performance of bubble imaging instrument described in this paper was compared with other instruments that were deployed in the ocean to estimate bubble size distribution, as given in Table I. It can be seen that the bubble imaging instrument is distinctive in its ability to measure a wide range of bubble sizes, small effective exposure time, and long recording time. It is therefore an improvement over historical cameras and provides new opportunities to gain insight into bubble formation and bubble populations.

VIII. Conclusion

We have presented the design and basic calibration of a bubble camera suitable for use underneath breaking waves in the open ocean. This camera was successfully used to collect open-ocean data during the HiWINGS campaign in 2013, and the automated image extraction code used to analyze that data has been published separately [33]. The design can be considered an update on the BubbleCam built by Stokes and Deane [25], after a complete reconsideration of the design decisions. The geometry and the lighting follow a similar principle, but we have added significant innovations in the hardware, software, and housing design creating an instrument with greater capability and application that is more robust. The hardware ensures that the data are captured at high resolution with low motion blur on to robust digital storage media, which can be transferred efficiently without the need to expose the internals of the instrument to harsh environments; the hardware allows the instrument to be operated autonomously over long durations and the software framework enables the capture profile to be customized to minimize energy consumption and maximize data saliency during long deployments; the T-shaped housing design makes the camera easy to secure to a free-floating platform, while ensuring the necessary isolation of the hardware and software within a single unit.

Acknowledgment

The authors would like to thank the officers and crew of *R/V Knorr* taking part in the HiWINGS campaign for their help during deployment of the bubble imaging instrument in the North Atlantic Ocean. The data from this paper can be obtained from University of Southampton e-Prints repository (http://doi.org/10.5258/SOTON/405186).

References

[1] D. M. Farmer, C. L. McNeil, and B. D. Johnson, "Evidence for the importance of bubbles in increasing air-sea gas flux," *Nature*, vol. 361, pp. 620–623, 1993.

[2] R. Wanninkhof, W. E. Asher, D. T. Ho, C. Sweeney, and W. R. McGillis, "Advances in quantifying air-sea gas exchange and environmental forcing," *Annu. Rev. Marine Sci.*, vol. 1, pp. 213–244, 2009.

[3] E. Fuentes, H. Coe, D. Green, G. de Leeuw, and G. McFiggans, "Laboratory-generated primary marine aerosol via bubble-bursting and atomization," *Atmos. Meas. Technol.*, vol. 3, no. 1, pp. 141–162, 2010.

[4] J. Zhou, K. Mopper, and U. Passow, "The role of surface-active carbohydrates in the formation of transparent exopolymer particles by bubble adsorption of seawater," *Limnol. Oceanogr.*, vol. 43, no. 8, pp. 1860–1871, 1998.

[5] H. Czerski, M. Twardowski, X. Zhang, and S. Vagle, "Resolving size distributions of bubbles with radii less than 30 m with optical and acoustical methods," *J. Geophys. Res.*, vol. 116, no. C7, pp. 1–13, 2011.

[6] H. Czerski, S. Vagle, D. M. Farmer, and N. Hall-Patch, "Improvements to the methods used to measure bubble attenuation using an underwater acoustical resonator," *J. Acoust. Soc. Amer.*, vol. 130, no. 5, pp. 3421–3430, 2011.

[7] P. J. Flatau, M. Flatau, J. R. V. Zaneveld, and C. D. Mobley, "Remote sensing of bubble clouds in sea water," *Quart. J. Roy. Meteorol. Soc.*, vol. 126, no. 568, pp. 2511–2523, 2000.

[8] R. Frouin, S. F. Iacobellis, and P.-Y. Deschamps, "Influence of oceanic whitecaps on the global radiation budget," *Geophys. Res. Lett.*, vol. 28, no. 8, pp. 1523–1526, 2001.

[9] J. Piskozub, D. Stramski, E. Terrill, and W. K. Melville, "Small-scale effects of underwater bubble clouds on ocean reflectance: 3-D modeling results," *Opt. Exp.*, vol. 17, no. 14, pp. 11747–11752, 2009.

[10] X. Zhang, M. Lewis, and B. Johnson, "Influence of bubbles on the scattering of light in the ocean," *Appl. Opt.*, vol. 37, no. 27, pp. 6525–6536, 1998.

[11] D. Stramski, "Gas microbubbles: An assessment of their significance to light scattering in quiescent seas," *Proc. SPIE*, vol. 2258, pp. 704–710, 1994.

[12] D. Stramski and J. Tegowski, "Effects of intermittent entrainment of air bubbles by breaking wind waves on ocean reflectance and underwater light field," *J. Geophys. Res.*, vol. 106, no. C12, pp. 31345–31360, 2001.

[13] E. J. Terrill and W. K. Melville, "A broadband acoustic technique for measuring bubble size distributions: Laboratory and shallow water measurements," *J. Atmos. Ocean. Technol.*, vol. 17, no. 2, pp. 220–239, 2000.

[14] M. A. Ainslie, "Effect of wind-generated bubbles on fixed range acoustic attenuation in shallow water at 1–4 kHz," *J. Acoust. Soc. Amer.*, vol. 118, no. 6, pp. 3513–3523, 2005.

[15] M. Y. Su, D. Todoroff, and J. Cartmill, "Laboratory comparisons of acoustic and optical sensors for microbubble measurement," *J. Atmos. Ocean. Technol.*, vol. 11, no. 1, pp. 170–181, 1994.

[16] M. D. Anguelova and P. Huq, "Characteristics of bubble clouds at various wind speeds," *J. Geophys Res.-Oceans*, vol. 117, no. C03036, pp. 1–22, 2012.

[17] H. Medwin, "In situ acoustic measurements of bubble populations in coastal ocean waters," *J. Geophys. Res.*, vol. 75, no. 3, pp. 599–611, 1970.

[18] H. Medwin, "In situ acoustic measurements of microbubbles at sea," *J. Geophys. Res.*, vol. 82, no. 6, pp. 971–976, 1977.

[19] G. Rojas and M. R. Loewen, "Void fraction measurements beneath plunging and spilling breaking waves," *J. Geophys. Res.*, vol. 115, no. C8, pp. 1–16, 2010.

[20] G. Rojas and M. R. Loewen, "Fiber-optic probe measurements of void fraction and bubble size distributions beneath breaking waves," *Exp. Fluids*, vol. 43, no. 6, pp. 895–906, 2007.

[21] B. Jähne and P. Geißler, "An imaging optical technique for bubble measurements," in *Proc. 3rd Int. Meeting Natural Phys. Processes Rel. Sea Surf. Sound*, Oakland, CA, USA, 1994, pp. 290–303.

[22] P. Geißler and B. Jähne, "Measurements of bubble size distributions with an optical technique based on depth from focus," in *Proc. Int. Symp. Air–Water Gas Transfer*, Heidelberg, Germany, 1995, pp. 351–362.

[23] I. Leifer, G. D. Leeuw, and L. H. Cohen, "Optical Measurement of Bubbles: System Design and Application," *J. Atmos. Ocean. Technol.*, vol. 20, no. 9, pp. 1317–1332, 2003.

[24] Q. Wang and E. C. Monahan, "The influence of salinity on the spectra of bubbles formed in breaking wave simulations," in *Proc. 3rd Int. Meeting Natural Phys. Processes Rel. Sea Surf. Sound*, 1994, pp. 312–319.

[25] M. D. Stokes and G. B. Deane, "A new optical instrument for the study of bubbles at high void fractions within breaking waves," *IEEE J. Ocean. Eng.*, vol. 24, no. 3, pp. 300–311, Jul. 1999.

[26] G. B. Deane and M. D. Stokes, "Air entrainment processes and bubble size distributions in the surf zone," *J. Phys. Oceanogr.*, vol. 29, no. 7, pp. 1393–1403, 1999.
[27] G. B. Deane and M. D. Stokes, "Scale dependence of bubble creation mechanisms in breaking waves," *Nature*, vol. 418, no. 6900, pp. 839–844, 2002.
[28] W. E. Asher and P. J. Farley, "Phase-Doppler anemometer measurement of bubble concentrations in laboratory-simulated breaking waves," *J. Geophys. Res.*, vol. 100, no. C4, pp. 7045–7056, 1995.
[29] R. W. Pascal *et al.*, "A spar buoy for high-frequency wave measurements and detection of wave breaking in the open ocean," *J. Atmos. Ocean. Technol.*, vol. 28, no. 4, pp. 590–605, 2011.
[30] T. G. Leighton, *The Acoustic Bubble*. London, U.K.: Academic, 1994.
[31] A. L. Walsh and P. J. Mulhearn, "Photographic measurements of bubble populations from breaking wind waves at sea," *J. Geophys. Res.*, vol. 92, no. C13, pp. 14533–14565, 1987.
[32] M. D. Anguelova and P. A. Hwang, "Whitecap fraction of actively breaking waves: Toward a database applicable for dynamic processes in the upper ocean," *18th Air-Sea Interact. Conf.*, vol. 9, pp. 1–13, 2012.
[33] R. S. Al-Lashi, S. R. Gunn, and H. Czerski, "Automated processing of oceanic bubble images for measuring bubble size distributions underneath breaking waves," *J. Atmos. Ocean. Technol.*, vol. 33, pp. 1701–1714, DOI: 10.1175/JTECH-D-15-0222.1.

Raied Sarmad Al-Lashi received the M.Sc. degree in electrical and electronic engineering from the University of Technology, Baghdad, Iraq, in 2002 and the Ph.D. degree in electronic engineering from the University of Nottingham, Nottingham, U.K., in 2012.

From 2013 to 2015, he was a Research Fellow in the Electronics and Computer Science, University of Southampton, Southampton, U.K. He is currently a Postdoctoral Research Associate at the University of Leeds, Leeds, U.K. His research interests include autonomous systems, instrumentation and meausrements, sensors, image and signal processing, and ultrasonic techniques for process monitoring and quality assurance.

Steve R. Gunn currently leads the Electronic and Software Systems research group in the Department of Electronics and Computer Science, University of Southampton, Southampton, U.K. He has published over 100 papers in the areas of image processing, machine learning, and embedded systems. From 2003 to 2013, he coordinated the EU Network of Excellence on Pattern Analysis, Statistical Modelling and Computational Learning (PASCAL and PASCAL2) which brought together the leading researchers across Europe in the areas of machine learning, statistics, and optimization.

Eric G. Webb received the B.Ed. degree in engineering and design and technology from King Alfreds's College Winchester, Winchester, U.K., in 1992.

During 1966–1970, he was a Mechanical Engineering Apprentice at Southampton Power station. During 1970–1990, he was an Engineering Technician at Marchwood Engineering Laboratories, Research and Development Facility for the Central Electricity Generating Board. He was involved in various projects including wave power test rigs, high-pressure steam boiler test rigs, and in-reactor inspection and repair for nuclear power stations. During 1992–1998, he was a Teacher in Horndean Community School. Since 1998, he has been a Technician in the Department of Electronics and Computer Science, University of Southampton, Southampton, U.K.

Helen Czerski received the B.A. and the M.Sci. degrees in natural sciences (physics) and the Ph.D. degree in physics from the University of Cambridge, Cambridge, U.K., in 2001 and 2006 respectively.

She is currently a Lecturer in the Department of Mechanical Engineering, University College London, London, U.K. She had worked in Los Alamos and at the Scripps Institution of Oceanography, the Graduate School of Oceanography in Rhode Island, and the University of Southampton, Southampton, U.K. Her research interest focuses on the bubbles formed by breaking waves in the open ocean.